CREEP PROPERTIES AND TEM CHARACTERIZATION OF 347H STAINLESS STEEL

B. Shalchi Amirkhiz[1], S. Xu[1], J. Liang[1] and C. Bibby[1]
[1] Natural Resources Canada, CanmetMATERIALS, Hamilton, Ontario, Canada
babak.shalchi_amirkhiz@canada.ca, su.xu@canada.ca, jie.liang@canada.ca,
catherine.bibby@canada.ca

Abstract

Creep properties of a recent 347H austenitic stainless steel plate at 1073 K (800°C) and 1123 K (850 °C) were examined, and microstructural evolution under temperature and creep was characterized using TEM. Creep minimum rate vs. stress plot at 1123 K (850 °C) showed two different slope regions, suggesting a change in the creep-rate controlling mechanism at lower stresses. Detailed TEM characterization showed that in high-stress (or short-term) creep tests, NbC precipitates interacted with dislocations and indicated to slow down the dislocation-controlled creep by orienting towards slip directions. In low-stress (long-term) creep tests, formation of ferrite on NbC was observed and no sigma phase was detected. In long-term low stress creep tests, NbC precipitates gave way to formation of Widmanstatten Cr_2N and Z-phase precipitates, and the rate-controlling mechanism may change to grain boundary sliding.

1. Introduction

The supercritical water-cooled reactor (SCWR) is a high temperature, high-pressure, light-water-cooled reactor concept considered by the Generation IV (Gen IV) reactor R&D program, that will operate above the thermodynamic critical point of water (647 K (374 °C), 22.1 MPa) [1]. Under envisaged service conditions, materials used in the components of the Gen IV SCWRs will operate beyond current service pressure and temperature regimes of Gen II and III nuclear reactors. Under these challenging conditions, a key issue regarding materials selection is adequate high-temperature mechanical and creep properties for structural components. Austenitic stainless steels are widely used in conventional and advanced reactors and the main compositions are with 15-20 wt. % Cr and 8-15 wt. %Ni balanced with Fe. Common commercial grades relevant to nuclear reactor applications are type 304, 316, 321, and 347 [2].

Niobium-stabilized austenitic stainless steel 347H (SS 347H) is a candidate alloy of interest for the Gen IV SCWRs [3]. In-depth understanding the high-temperature mechanical and creep properties and microstructural evolution of 347H is essential in view of the challenging design conditions of the proposed SCWR. In general, high-temperature mechanical properties and phase stability of stainless steels is linked to formation, dissolution and coarsening of precipitates [4]. In solution-annealed condition, 347H contains Nb and C within the matrix, which will precipitate during aging to form MC type niobium carbide [2,5]. These precipitates stabilize the steel against grain boundary precipitation of $M_{23}C_6$ type carbides which cause sensitization. Nb-stabilized stainless steels also present improved creep property compared with typical non-stabilized grades and can be used in elevated temperature applications up to 1123 K (850 °C) where a combination of creep strength and resistance to intergranular corrosion is critical [2,3,6,7]. The undesirable formation of ferrite in high

temperature creep of 347H is probable, and it could be prevented by addition of alloying elements such as B and Ce [8]. The intermetallic σ-phase, which is a brittle body-centered tetragonal phase, could form in stainless steels at a much slower rate than MC carbides, which can result in performance degradation [2,9]. Another precipitation that might form during creep of stainless steels is CrNbN or Z-phase which has been covered extensively in the literature regarding creep in Nb bearing stainless steels; albeit with no consensus on its origins [10–14].

Creep data at temperatures up to 1123 K (850 °C) are of interest for Gen IV SCWR fuel cladding application, and such data at 1123 K (850 °C) were not available in the open literature. In this work, high-temperature tensile tests of a commercial SS 347H plate were performed up to 1273 K (1000 °C); creep tests were performed at 1073 K (800 °C) and 1123 K (850°C) to fill creep data gaps and to validate creep rupture prediction results using the Larson-Miller Parameter (LMP) with an optimized LMP constant reported in [3]. Precipitation and deformation behaviours in the as-received aged, and creep conditions were examined using transmission electron microscopy (TEM). In this paper, creep properties will be reported and briefly discussed; the focus of this paper will be on TEM characterization of microstructure of creep tested specimens. Detailed results of high-temperature mechanical properties and additional creep analysis will be reported elsewhere.

2. Materials and Methods

A commercial flat-rolled plate of 347H with a thickness of 25.4 mm and in a standard solution-treatment condition (1373K, 30 min) was purchased and used in this study. Spectrography was performed to confirm the composition and showed good agreement with the mill report. Compositions of the material are given in Table 1. Note that the carbon content of the 347H is at the low level of the composition specification of 347H.

Table 1 Chemical composition of the 347H plate used in this study (in wt. %).

Alloy	Element	C	Mn	P	S	Cr	Ni	Mo	Cu	Nb	Ti	Si	N	Co
347H	Mill report	0.04	1.67	0.036	0.001	17.1	9.13	0.44	0.34		0.005		0.017	
	Spectrography	0.04	1.70	0.035	0.005	17.3	9.0	0.36	0.31	0.36	0.005	0.40	0.018	0.12

Creep specimens were machined from the as-received plates in the solution-treatment condition and were close to the middle thickness of the plate. Most creep specimens were taken from transverse orientation to the rolling direction. Creep specimens were cylindrical with a gauge length of 63.5 mm and diameter of 6.35 mm. Creep tests were carried out at 1073 K (800 °C) and 1123 K (850 °C). For optical characterization, Glyceregia etchant was used. Based on metallographic examination, the microstructure is uniform through thickness. Optical micrographs of the as-received material are shown in Fig. 1. The microstructure of the as- received 347H showed equiaxed grain structure and anneal twining.

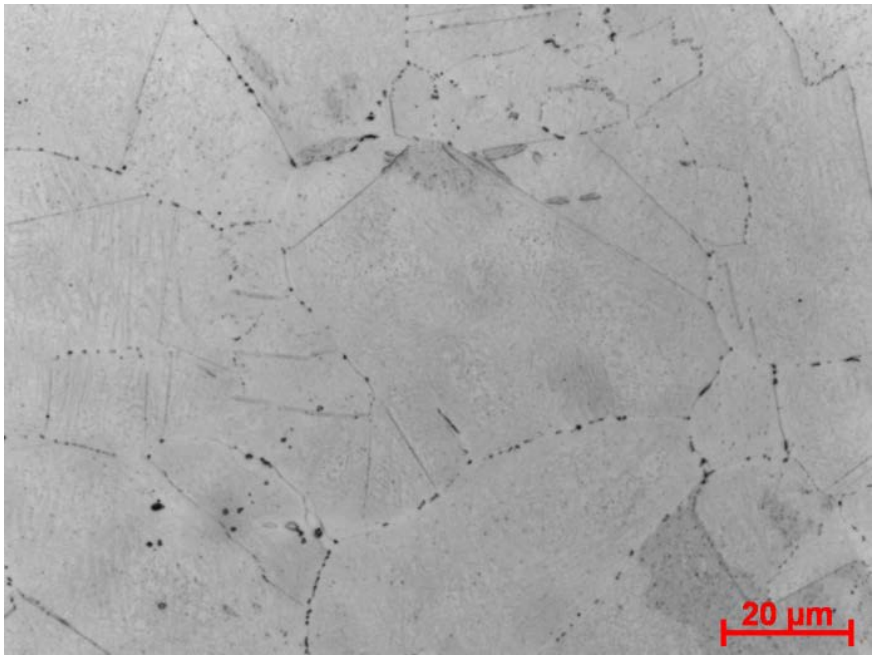

Figure 1 Optical micrograph showing a transverse cross section of the as-received 347H.

The microstructure of as-received and crept samples was examined using a FEI Tecnai Osiris transmission electron microscope (TEM) operating at 200 kV. Conventional bright field – dark field imaging and diffraction techniques were used for general characterization and phase identification. Scanning mode (STEM) using a high-angle annular dark-field (HAADF) detector was used to generate Z-contrast imaging and energy-dispersive X-ray spectroscopy (EDX). Quantitative EDX measurement in combination with diffraction was used for phase identification, and EDX elemental mapping was used to characterize precipitates. For TEM investigations, foil samples were made by punching out 3 mm discs and then grinding and dimpling them to a desired center thickness (approx. 10 µm), followed by ion milling (Gatan PIPS). The TEM study was done on the as-received sample, a sample aged for 1244.2 hours at 1123 K (850 °C), and on samples crept under 40.0, 30.5 and 20.4 MPa with creep life of 1244.2, 2265.1 and 9595.2 hours respectively at 1123 K (850 °C). For the creep test specimens, TEM samples were selected from regions away from the fracture area.

3. Results and Discussion

3.1 Creep properties

Creep rupture tests were carried out in transverse and longitudinal samples at 1073 K (800 °C) and 1123 K (850 °C). Typical creep strain vs. time curves of the transverse samples crept at 1123 K (850 °C) are shown in Fig. 2. These plots demonstrate the typical primary, secondary and tertiary stages of creep in the 347H and show a considerable creep strain at higher stresses. Also, the extent of the secondary creep stage at high stresses was limited. A prolonged tertiary creep stage was observed for lower stresses. The creep properties of 347H – rupture life (t_r), minimum creep rate ($\dot{\varepsilon}$) and creep elongation – are summarized in Table 2.

Table 2 Creep properties

T (K)	Stress (MPa)	t_r (h)	Min. rate (/s)	Elongation (%)
1123	80	31.5	6.3E-7	43.3
	64.5	127.6	7.1E-8	19.0
	59.9	228.1	3.9E-8	15.6
	49.8	627.8	1.4E-8	14.3
	40.0	1244.2	8.0E-9	11.8
	30.5	2265.1	1.8E-9	9.3
	20.4	9595.2	1.4E-9	26.3
	49.8 (Longitudinal)	545.8	7.9E-9	8.1%
1073	80	272.6	3.26E-8	29.4
	60	1729.3	3.1E-9	10.7
	50	3881.2	8.9E-10	7.2

Minimum creep rate vs. stress relationship of the 347H steel is shown in Fig. 3. Minimum creep rate is often expressed as a power law equation of stress,

$$\dot{\varepsilon}_m = A\sigma^n \exp\left(-Q/RT\right) \qquad (1)$$

where $\dot{\varepsilon}_m$ is the minimum creep rate, A is constant, σ is the applied stress, n is the creep stress exponent, Q is the activation energy and R is the gas constant. It is well established that for pure metal and metals behaving similar to pure metals, n is constant and is close to 5 (hence five-power-law behavior). For alloys, n values may be higher than 5 due to other strengthening mechanisms. The n value is approximately 7.1 for creep at 1073 K (800 °C); for creep at 1123 K (850 °C), the data indicate two slopes, i.e. 2.4 for the lower stress region and 8.1 for the higher stress region, respectively. The n values of 7.1 and 8.1 are typical for 347H (e.g., [11,15,16]) and for intragranular dislocation creep phenomenon of alloys. The n value of 2.4 is close to that for grain boundary sliding.

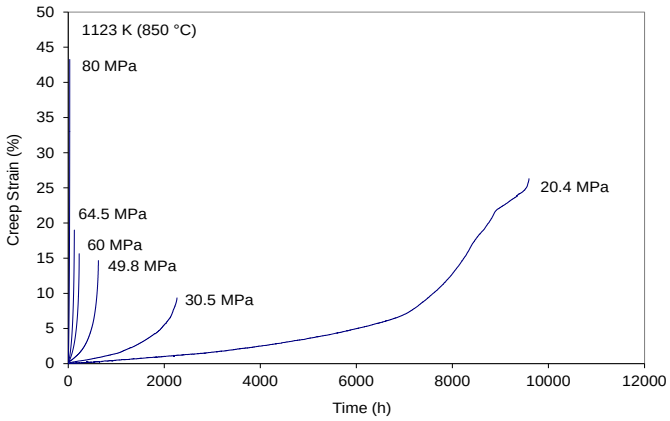

Figure 2 Creep strain vs. time curves of 347H at 1123 K (850 °C).

Change of stress exponent values on lowering the stress seen in Fig. 3 were examined through TEM microstructural observations to try to correlate the creep behavior to the microstructure in next section. At lower stresses, dislocations and their interaction with precipitates were dominant due to extensive precipitations. It could be that the rate-controlling mechanism changes from an intragranular dislocation creep mechanism at high stresses (or short durations) to a grain boundary sliding controlled creep when the stress component value changes from n=8.1 to n= 2.4 at lower stress values. Grain boundary sliding as a deformation mechanism during creep has been studied extensively in the past and has been presented as a major operating mechanism in creep deformation at low stresses and / or small grain sizes [17–20]. Contribution of grain boundary sliding in creep deformation of 347 has been previously characterized [21].

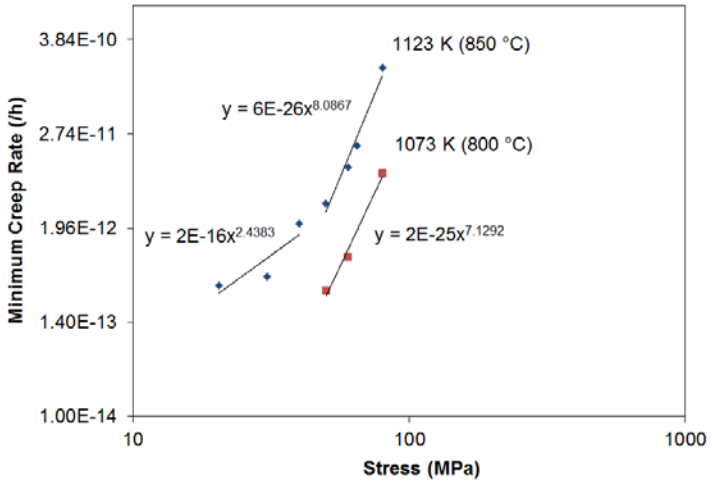

Figure 3 Minimum creep rate vs. stress of 347H.

3.2 TEM characterization

The TEM study was done on the as-received sample, a sample aged for 1244.2 hours at 1123 K (850 °C), and on samples crept at 1123 K (850 °C) under 40.0, 30.5 and 20.4 MPa with creep life of 1244.2, 2265.1 and 9595.2 hours, respectively. Figure 4 shows that niobium carbide particles were present within the gamma matrix and also at grain boundaries in the as-received sample.

TEM observation of niobium carbide particles in samples having undergone creep revealed how precipitates react to stress/temperature and how they interact with dislocations. By tilting the TEM sample so that the electron beam is parallel to the <011> zone axis, some interesting features were revealed. As seen in Fig. 5a, slip lines are seen within the grains in <111> directions in a sample that has undergone creep under 40.0 MPa at 1123 K (850 °C) for 1244.2 h. As shown in Fig. 5b, the cubic carbide precipitates are aligned towards <111> directions as well. A coherent niobium carbide is seen in the high-resolution STEM-HAADF image shown in Fig. 5c and the corresponding EDS map is displayed in Fig. 5d. A step created in the particle is indicative of dislocation cutting attributed to dislocation climb over coherent particles [22].

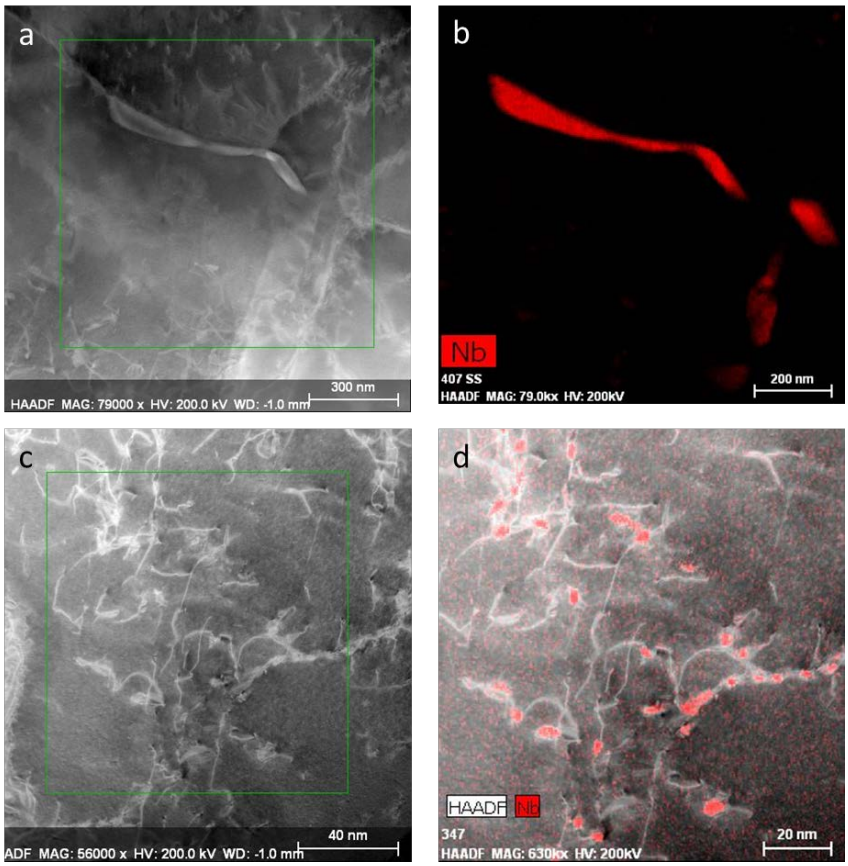

Figure 4 STEM / HAADF images and corresponding Nb elemental maps showing Nb-C precipitation in grain boundaries (a-b) and at dislocations within the grains (c-d) in the as- received material.

The fringes in Fig. 5c are scanning moiré fringes (SMF) which are a product of spatial interference between the scanning grating of the electron beam in STEM mode and the specimen atomic lattice [23]. While the SMF shows no deformation within the carbide particle, a severe deformation is manifested in the form of irregular moiré fringes within the gamma matrix. One interesting feature of the moiré fringes is that they can magnify the irregularities or defects within a pattern. This phenomenon is shown in Fig. 5c, where magnified images of the dislocations within the gamma matrix are visible within the SMF. A stress field revealed by the SMF around the NbC particle is another indication of dislocation climb over coherent particles [22].

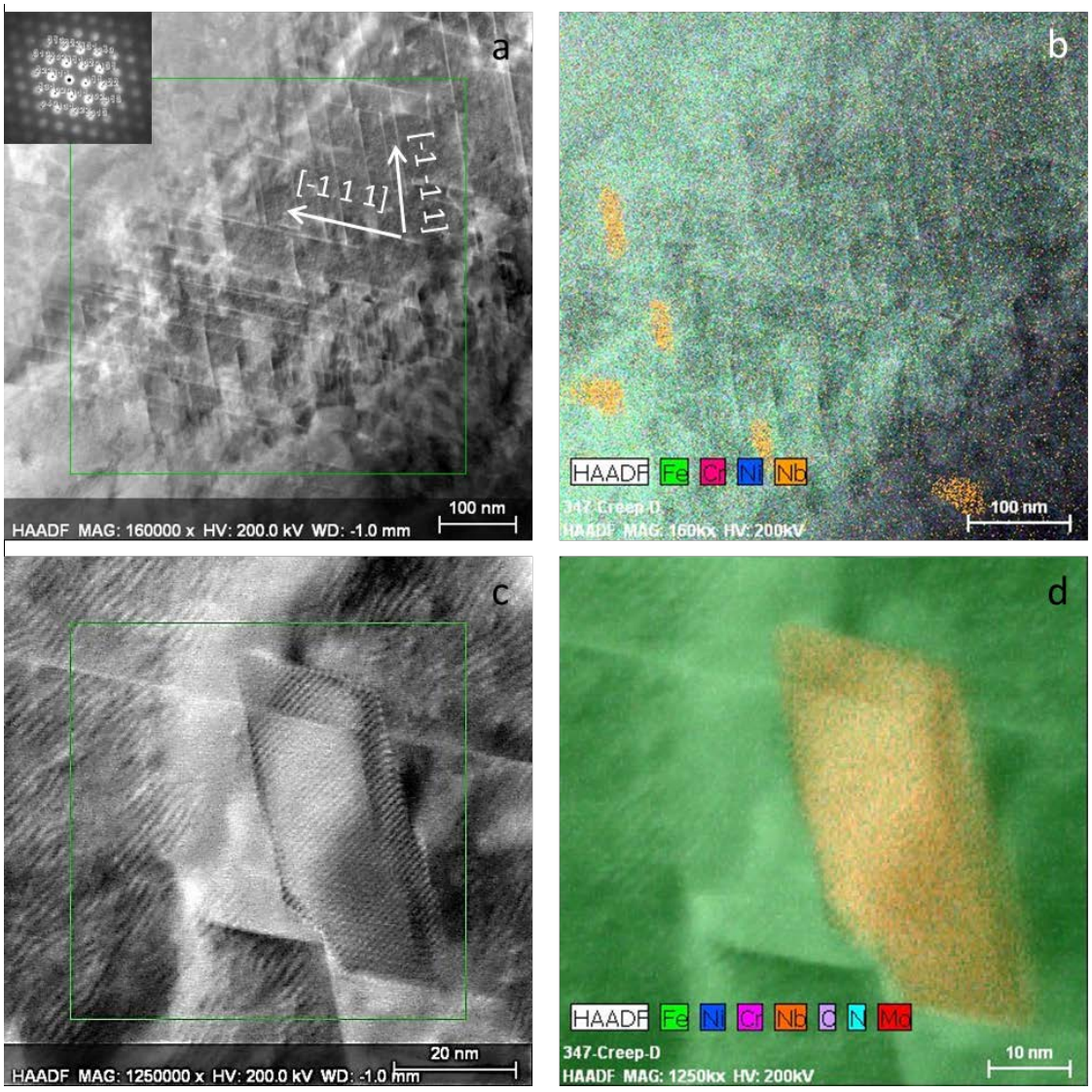

Figure 5 TEM of the sample crept under 40 MPa for 1244.2 hours at 1123 K (850 °C). (a) STEM-HAADF image taken in <011> zone axis showing slip lines; (b) the corresponding EDS elemental map showing NbC precipitates of image (a); (c) high-resolution STEM-HAADF image showing an NbC precipitate oriented towards slip direction cut by a dislocation. Scanning moiré fringes magnify deformation within the matrix around the precipitate; and (d) the corresponding EDS elemental map of the image.

The ability of the SMF to display creep deformation becomes more evident when comparing the image in Fig. 5c with a similar image shown in Fig. 6a from a sample taken out of the grip section of the creep test specimen. In this sample, the material has not undergone creep deformation, but experiences the same temperature regime as the creep sample (aged for 1244.2 hours at 1123 K (850 °C)). The moiré fringes illustrate much less deformation and only a few dislocations are visible (the arrows in Fig. 6a). Note that the dash lines show the interface between an NbC carbide particle and the matrix; and the carbide particle does not show any sign of deformation.

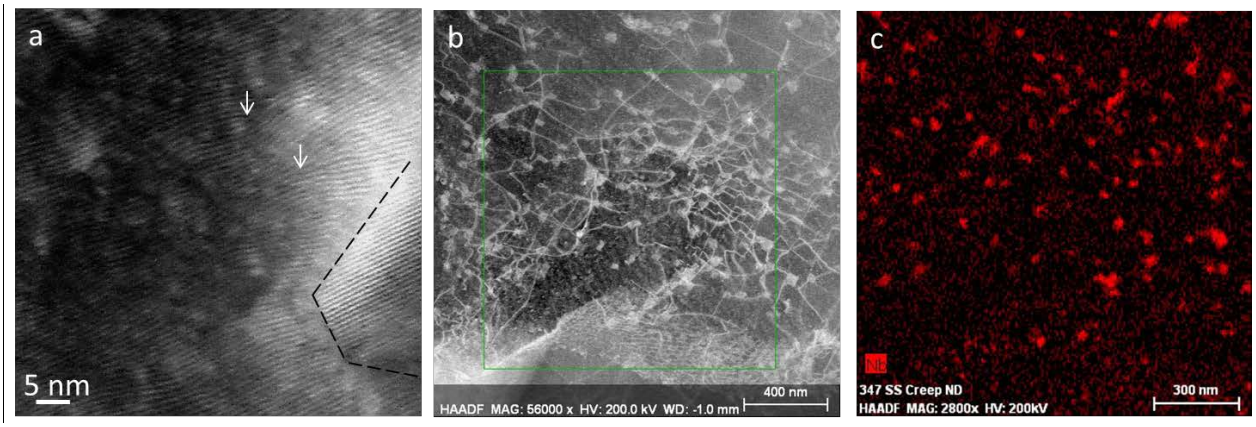

Figure 6 TEM of the sample aged for 1244.2 hours at 1123 K (850 °C). (a) STEM-HAADF image showing scanning moiré fringes in a carbide particle and the gamma matrix; (b) STEM-HAADF image showing interaction between NbC precipitates and dislocations; (c) the corresponding Nb elemental map of image (b).

Another microstructural feature seen in the aged sample was dislocation pinning by NbC precipitates as can be seen in Fig. 6b. Diffraction study of the carbide precipitate revealed the structure as cubic NbC, as shown in Fig. 7 where the selected area diffraction pattern and corresponding TEM bright field images are shown along with a dark field image formed using $(\bar{1}\bar{1}\bar{1})$ reflection of an NbC precipitate. Strain contours seen in the bright field image in Fig 7(b), are indicative of dislocation climb over coherent particles.

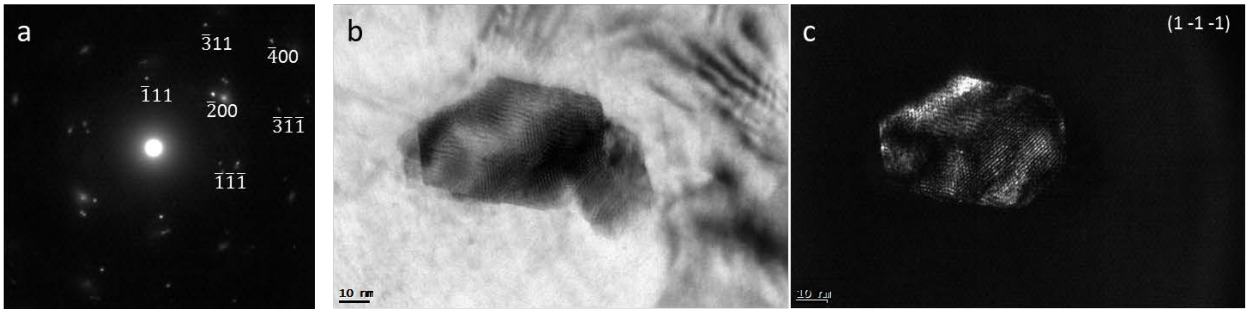

Figure 7 Electron diffraction pattern (a) and corresponding TEM bright-field (b) and dark-field (c) images showing a cubic NbC precipitate. The dark-field image is formed using (1 -1 -1) reflection of the NbC particle. The scale bar is 10 nm.

The TEM study of the sample having undergone creep under 30.5 MPa at 1123 K (850 °C) with creep life of 2265.1 hours revealed formation of δ-ferrite within the gamma matrix as can be seen in Fig. 8. Formation of ferrite in stainless steels is generally considered undesirable. It has been reported that ferrite precipitate can nucleate on residual $M_{23}C_6$ and chromic oxide particles within the gamma matrix and subsequently could undergo a transformation into sigma phase [24]. The ferrite grain seen in Fig. 8 has nucleated on an NbC precipitate as evident in Fig. 9.

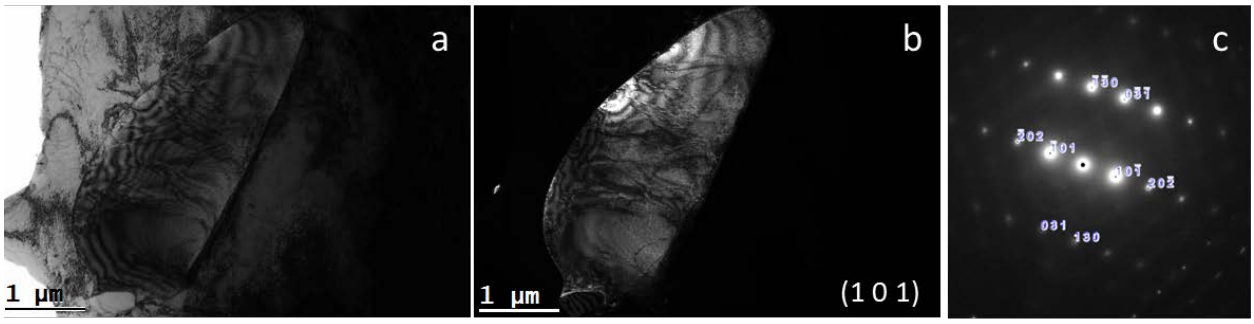

Figure 8 A δ-ferrite grain (BCC) formed within the gamma matrix of the sample crept under 30.5 MPa at 1123 K (850 °C) for 2265.1 hours; (a) bright field (b) TEM dark field from (101) reflection and (c) corresponding SAD at <313> zone axis of alpha.

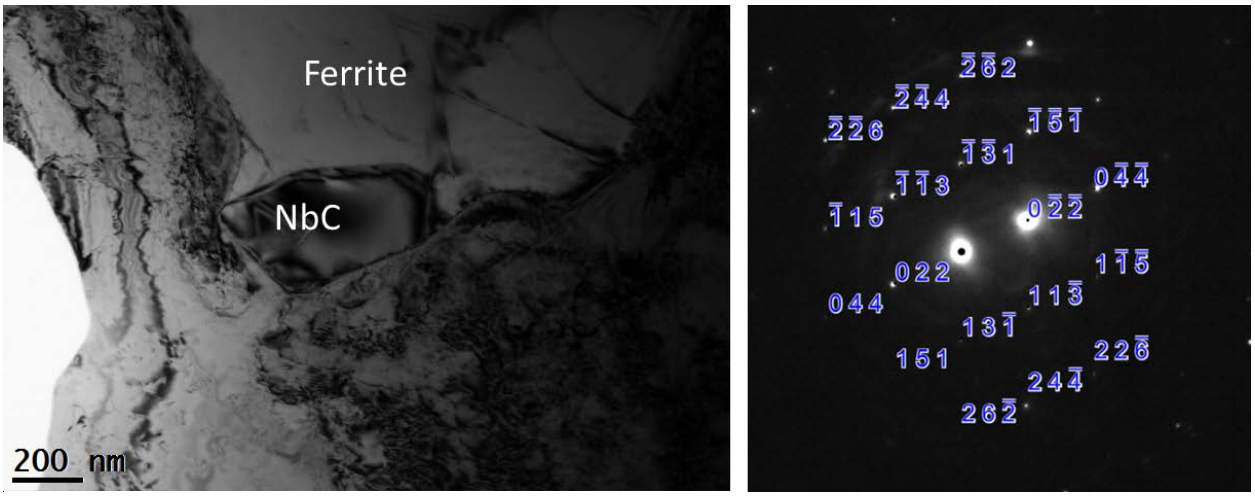

Figure 9 The ferrite grain shown in Fig. 13 has nucleated from an NbC precipitate. The diffraction pattern is the corresponding SAD showing <411> zone axis of NbC.

EDS analysis showed a high concentration of Cr in the ferrite grain (23 wt. %) which hints eventual transformation into σ (approx. 50 wt. % Cr). However, no sigma phase was found in the prolonged creep test materials, which suggests that either the formation of ferrite was limited or transformation of ferrite to sigma did not occur. It has been reported that N could suppress formation of δ-ferrite [8], and as will be shown in the following, there has been significant N uptake in prolonged creep tests.

TEM also showed severe creep deformation in the form of slip lines and stacking faults. Slip traces are shown in Fig. 10a and examples of stacking faults are shown in Fig. 10b. It is important to note that in regions where there was a high density of NbC precipitates traces of slip were less evident and dislocations were found entangled with the precipitates; many of them were bowed indicating dislocation climb over incoherent precipitates; subgrain boundaries have formed (Fig. 11) which were absent in the sample crept under 40 MPa. This is attributed to the incoherency of the precipitates in this sample which has resulted in facilitated dislocation movement as opposed to the sample crept under 40 MPa were coherent NbC particles seen to be cut with dislocations.

Dislocation climb over coherent precipitates occurs through cutting which requires more energy than climb over incoherent precipitates [22].

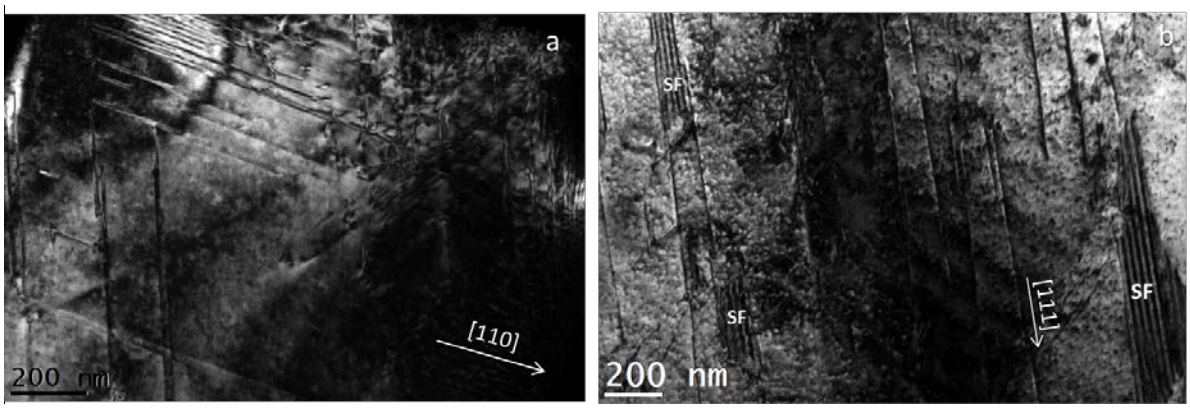

Figure 10 TEM micrographs showing (a) traces of slip and (b) stacking faults (SF) in the sample crept under 30.5 MPa at 1123 K (850 °C) for 2265.1 hours.

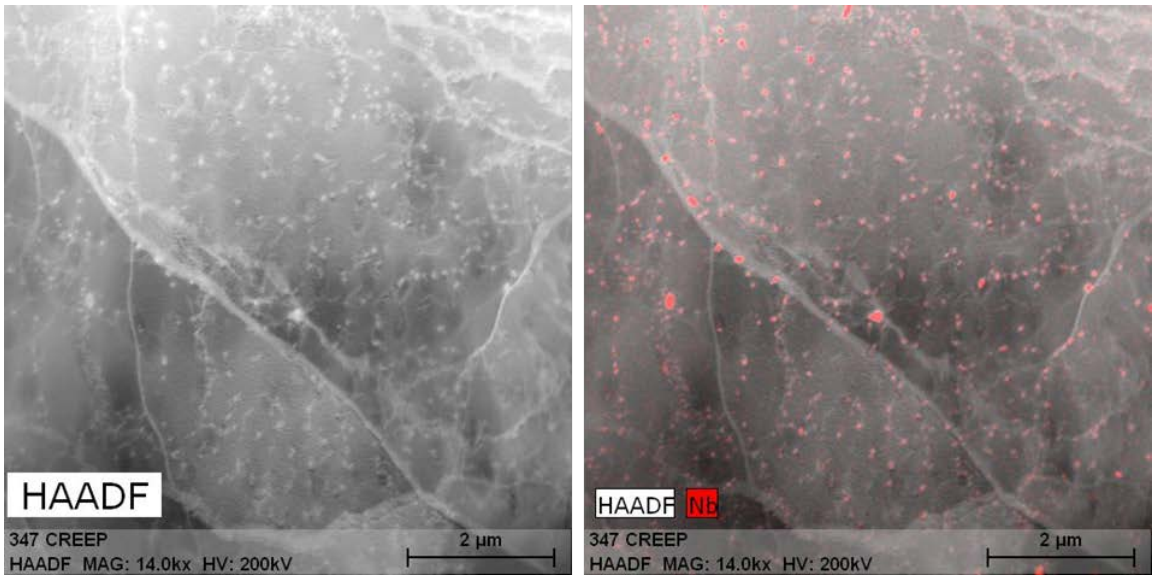

Figure 11 HAADF image and HAADF/Nb elemental map overlay from a region with high density of NbC precipitates. No trace of slip is seen; subgrain formation is seen. The sample crept under 30.5 MPa at 1123 K (850 °C) for 2265.1 hours.

Optical micrographs showed sever wedge-type cavity formation throughout the bulk of the 9595.2 hours crept sample in the vicinity of fracture surface shown in Fig 12(a). Cavity formation can be indicative of grain boundary sliding [25–27]. A two-power stress relationship at low stresses is rationalized for grain boundary sliding [28,29]; which is in accord with the measured value in the low stress region (Fig 3). Moreover, as a result of cavitation, nitrogen diffusion from air into the bulk of sample resulted in formation of an extensive network of Cr_2N precipitates in the vicinity of the cavities as seen in Fig 12(b). TEM observation of these precipitates revealed an extensive network of Widmanstatten chromium nitride precipitates as can be seen in Fig. 13. The Widmanstatten chromium nitride precipitates ranged between 600 nm to 10 µm in size and oriented

towards <111> within the matrix, where equiaxed Cr-N precipitates were found at grain boundaries (not shown here).

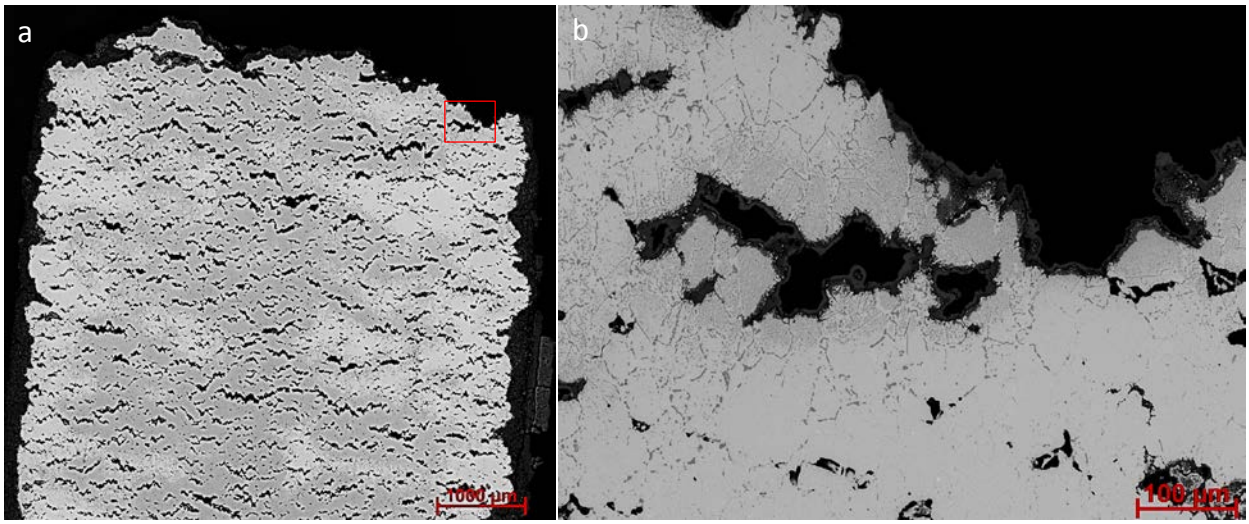

Figure 12 Optical cross sectional images showing the extent of cavity formation in the vicinity of the fractured surface of the sample crept under 20.4 MPa at 1123 K (850 °C) for 9595.2 hours (a), and formation of Cr_2N around cavities in the highlighted area (b). Areas with Cr_2N precipitates are seen as greyer areas around cavities in (a).

The gamma matrix in this sample is Cr-depleted; EDS measurements showed the composition as approximately 10 wt.% Ni, 7% Cr, 2.5% Mn, 0.5% Si and balance Fe. Formation of Widmanstatten chromium nitride in stainless steels has been reported in the literature [30]. Diffraction study of the chromium nitride precipitation along with quantitative EDS confirmed Cr_2N structure as shown in Fig. 14. Nitrogen uptake and formation of Cr_2N precipitates during prolonged creep in Nb-stabilized 347H has previously been reported for creep at 1073 K (800 °C) for 77,782 h, and a sharp loss of ductility has been attributed to N uptake [31].

The niobium carbide precipitates in this sample had a bimodal size distribution as can be seen in the Nb map in Fig. 13. Diffraction study on the larger Nb precipitates revealed the crystal structure of the carbide as NbC, as shown in Fig. 15. NbC particles in Fig. 15a are at the core of Cr_2N precipitates. This could be evidence of nucleation of Cr_2N phase on NbC particles.

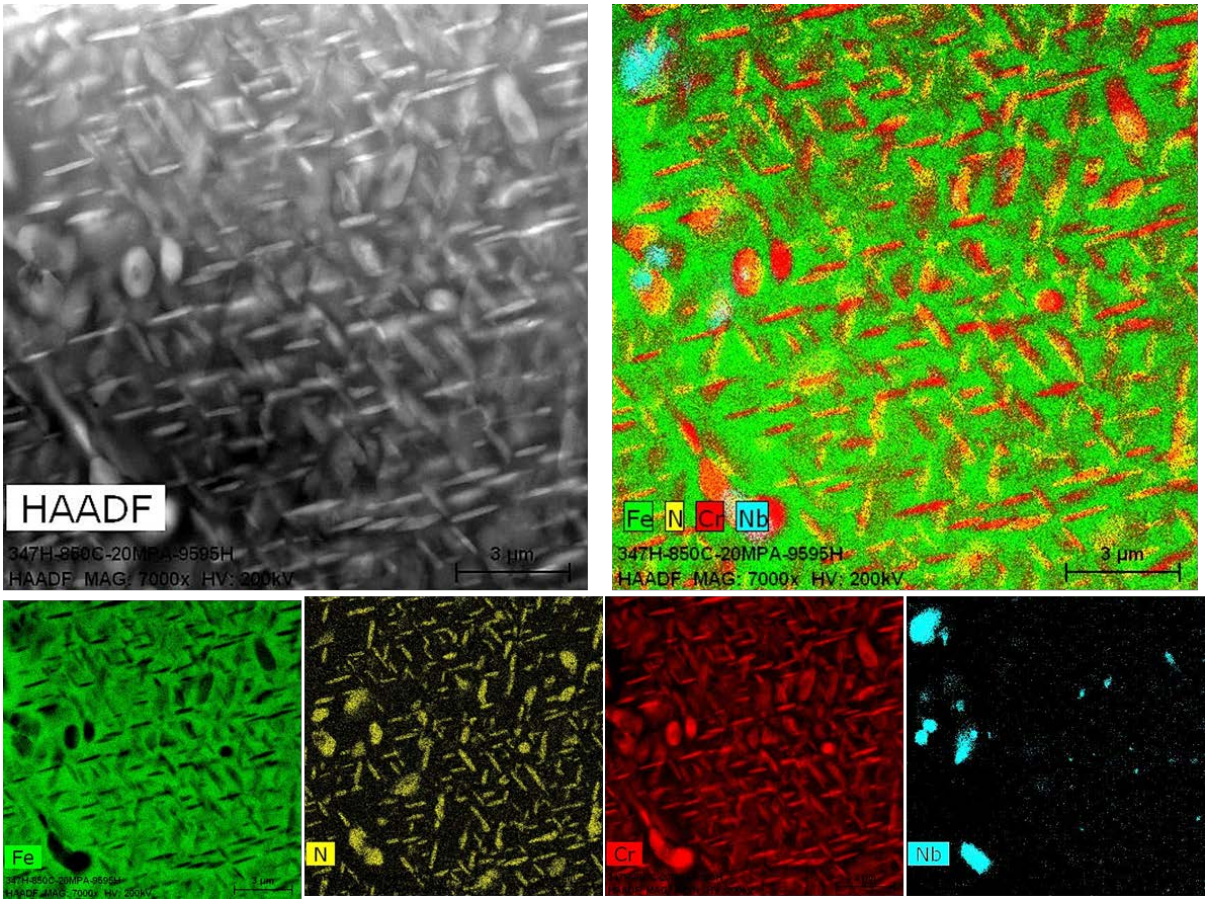

Figure 13 HAADF and corresponding elemental maps of Fe, N, Cr and Nb showing an extensive network of Widmanstatten chromium nitride precipitates in the sample crept under 20.4 MPa at 1123 K (850 °C) for 9595.2 hours.

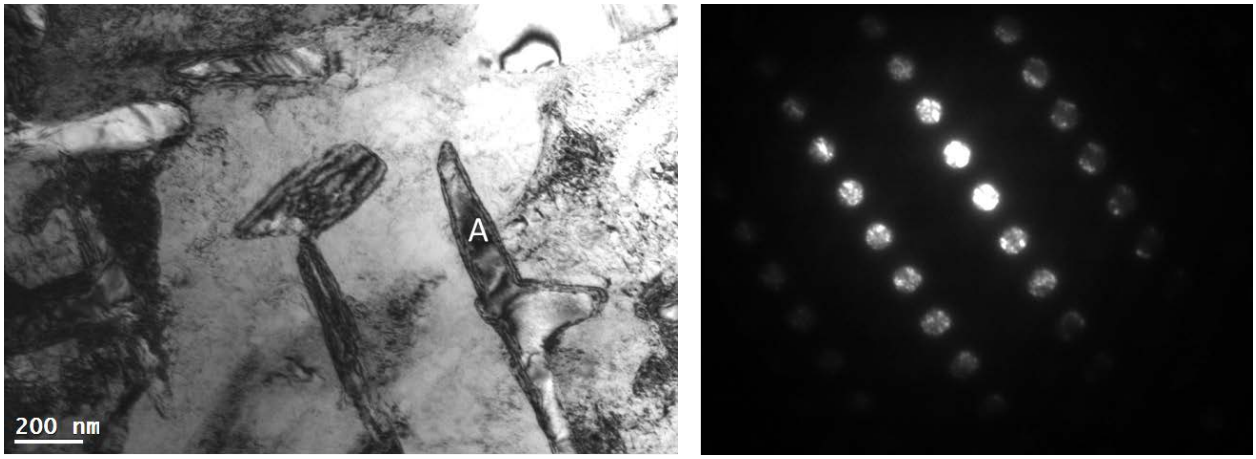

Figure 14 TEM bright field showing Widmanstatten chromium nitride precipitates within the gamma matrix and CBED pattern acquired from spot A showing Cr_2N. Sample crept under 20.4 MPa at 1123 K (850 °C) for 9595.2 hours.

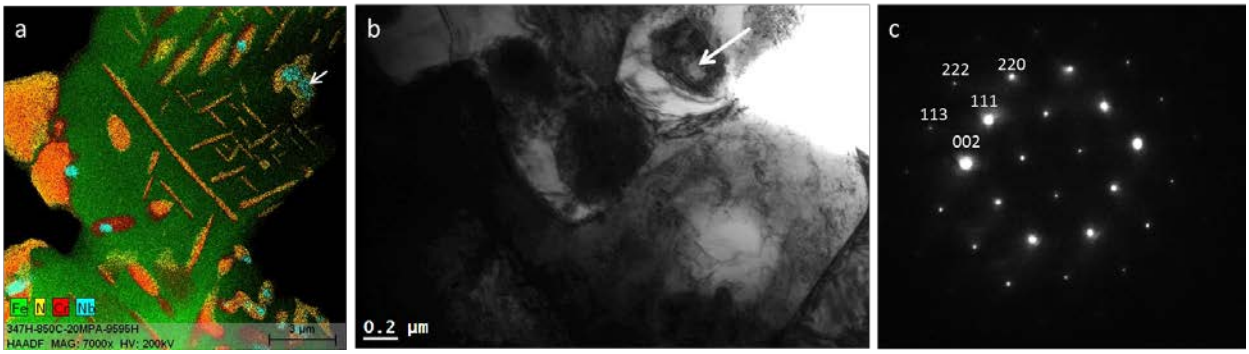

Figure 15 EDS elemental map (a) showing Widmanstatten Cr2N precipitates and niobium particles (blue precipitates), TEM bright field image (b) taken from the region marked with an arrow in (a), and SAD pattern (c) taken from arrowed precipitate in (b), showing cubic NbC with the beam oriented towards its <110> zone axis. The NbC particle is in the core of a Cr_2N precipitate. Sample crept under 20.4 MPa at 1123 K (850 °C) for 9595.2 hours.

Closer study of the niobium-bearing precipitates of smaller size revealed that they contained N and Cr as evident in Fig. 16, and are of Z-phase nature. The very small size of the Z-phase precipitates suggests they are at initial state of nucleation and growth. Different mechanisms for formation of Z-phase have been suggested in the literature, such as through diffusion of Cr and N into MX (NbC) or M_2X (Cr_2N) [10,11,14]. Precipitates of Z-phase are deemed to increase resistance against creep deformation in stainless steels [12]. A summary of microstructural observations is given in Table 3.

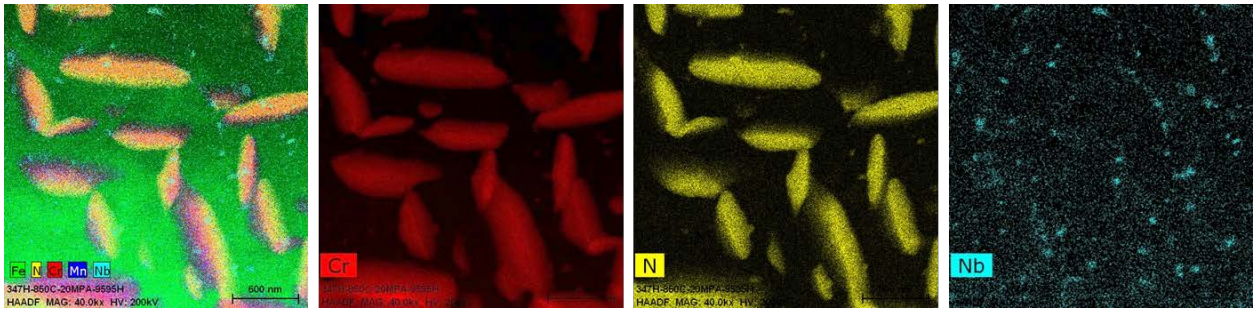

Figure 16 EDS elemental combination map showing Cr2N precipitates along with elemental maps of Cr, N and Nb revealing smaller Z-phase precipitates within the matrix of the sample crept under 20.4 MPa at 1123 K (850 °C) for 9595.2 hours.

Table 3 Summary of microstructural observations

T [K]	Stress [MPa]	Time [h]	Observed precipitates	Microstructural features
RT	0	-	NbC	Precipitation at grain boundaries and on dislocations within the matrix
1123	0	1244.2	NbC	Less precipitation at grain boundaries, dislocation movement and pinning at precipitates
1123	40.0	1244.2	NbC	Severe deformation, slip, NbC precipitates oriented towards slip directions
1123	30.5	2265.1	NbC, δ-ferrite	Nucleation Cr-rich δ-ferrite on NbC, stacking faults, slip
1123	20.4	9595.2	NbC, Cr_2N, Z-phase	Widmanstatten Cr_2N, nanometric Z-phase

4. Conclusions

Creep tests were carried out at 1073 K (800 °C) and 1123 K (850 °C) and in-depth TEM examinations were performed on as-received and crept specimens. The following conclusions can be made:

- Creep minimum rate vs. stress plot at 1123 K (850 °C) shows two different slope regions. The creep mechanism may change from an intragranular dislocation creep mechanism at high stresses to a grain boundary sliding controlled creep when the stress component value changes from n=8.1 to n= 2.4 at lower stress values. This was studied in this work with optical microscopy and TEM.
- At high stresses, dislocations are found to be entangled with NbC precipitates and hence their motion controls the creep rate. The observed stacking faults within the matrix of the crept samples at higher stresses are indicative of dislocation climb and therefore the five-power-law creep.
- Slip lines and stacking faults were observed in regions where the density of NbC precipitates was lower in medium life creep samples (at 40 and 30 MPa). No sub-grain boundary as a result of dislocations re-arrangement was observed.
- At low stress levels at prolonged creep, dislocations were not found to be the dominant feature. Optical microscopy observation of cavitation in the sample crept under 20.4 MPa suggested grain boundary sliding as the operating creep mechanism. Cavitation is a result of grain boundary sliding.
- At 30.5 MPa where creep life was longer, Cr-rich δ-ferrite was observed to nucleate on NbC particles. Although this was reported as a prelude to formation of σ-phase, no such phase was detected in any of the samples. Nitrogen uptake could be responsible for suppressing further δ-ferrite and σ-phase formation.

- At the lowest creep stress level tested (20.4 MPa) with the creep life of 9595.2 hours, an extensive network of cavities formed, where precipitation of Cr_2N phase with Widmanstatten morphology within the matrix and large equiaxed Cr_2N particles at grain boundaries were observed. Cr_2N phase nucleated at NbC precipitates upon nitrogen uptake from the surface and through the cavities. Precipitation of Z-phase was also observed in the longest creep at 1123 K (850 °C).
- NbC precipitates were shown to be effective in reducing the creep rate by pinning dislocations or aligning themselves towards slip directions which is evident by step formed on the coherent precipitates and bowed dislocations around incoherent ones in low and medium creep life samples (30 and 40 MPa).

5. Acknowledgements

This work forms part of CanmetMATERIALS (CMAT) projects on high-temperature mechanical properties of reactor materials. The projects are supported by the Next Generation Nuclear Program, part of the Canadian Interdepartmental Program of Energy Research and Development (PERD) and the ecoENERGY Innovation Initiative (ecoEII) funding. The Program of Energy Research and Development (PERD) committee members, especially Dr. W. Zheng (also Program Manager of Materials for Energy Production at CMAT), are gratefully acknowledged for their comments and guidance in the work. We also would like to thank P. Liu and R. Zavadil for metallographic examination.

6. References

[1] T.R. Allen, K. Sridharan, Y. Chen, L. Tan, X. Ren, A. Kruizenga, Materials development and selection for corrosion resistance. A critical issue in supercritical water reactors, in: 16th Pacific Basin Nucl. Conf. Pacific Partnersh. Towar. a Sustain. Nucl. Futur., Atomic Energy Society of Japan, Tokyo, Japan, 2008: pp. 2022–2027. doi:16PBNC: 16.

[2] P.J. Maziasz, J.T. Busby, Properties of austenitic steels for nuclear reactor applications, Compr. Nucl. Mater. 2 (2012) 267–283. doi:10.1016/B978-0-08-056033-5.00019-7.

[3] S. Xu, S.-M. Jin, P. Le Dreff-Kerwin, Mechanical property database development and creep prediction of candidate generation IV SCWR alloys, in: ASME Press. Vessel. Pip. Conf., ASME, Paris, 2013: p. V06BT06A002. doi:10.1115/PVP2013-97290.

[4] T. Sourmail, Precipitation in creep resistant austenitic stainless steels, Mater. Sci. Technol. 17 (2001). doi:10.1179/026708301101508972.

[5] J. Källqvist, H.-O. Andrén, Microanalysis of a stabilised austenitic stainless steel after long term ageing, Mater. Sci. Eng. A. 270 (1999) 27–32. doi:10.1016/S0921-5093(99)00234-8.

[6] J.O. Nilsson, Prediction of Properties in Type 347 Austenitic Stainless Steel after Long-Term Service at High Temperatures, Mater. Sci. Forum. 539-543 (2007) 4920–4925. doi:10.4028/www.scientific.net/MSF.539-543.4920.

[7] L.K. and A.R. D. D'Angelo, E. Evangelista, S. Spigarelli, Creep of Cold Deformed AISI 347

Stainless Steel, in: Fifth Int. Conf. Creep Mater., Lake Buena Vista, 1992: pp. 127–133.

[8] Y. Xu, H. Nie, J. Li, X. Xiao, C. Zhu, J. Zhao, Growth of creep life of type-347H austenitic stainless steel by micro-alloying elements, Mater. Sci. Eng. A. 528 (2010) 643–649. doi:10.1016/j.msea.2010.09.086.

[9] J. Erneman, M. Schwind, L. Nylöf, J.-O. Nilsson, H.-O. Andrén, J. Ågren, Comparison between quantitative metallography and modeling of σ-phase particle growth in AISI 347 stainless steel, Metall. Mater. Trans. A. 36 (2005) 2595–2600. doi:10.1007/s11661-005-0257-2.

[10] D.B. Park, M.Y. Huh, W.S. Jung, J.Y. Suh, J.H. Shim, S.C. Lee, Effect of vanadium addition on the creep resistance of 18Cr9Ni3CuNbN austenitic stainless heat resistant steel, J. Alloys Compd. 574 (2013) 532–538. doi:10.1016/j.jallcom.2013.05.106.

[11] D.-B. Park, S.-M. Hong, K.-H. Lee, M.-Y. Huh, J.-Y. Suh, S.-C. Lee, et al., High-temperature creep behavior and microstructural evolution of an 18Cr9Ni3CuNbVN austenitic stainless steel, Mater. Charact. 93 (2014) 52–61. doi:10.1016/j.matchar.2014.03.012.

[12] K.-H. Lee, J.-Y. Suh, J.-Y. Huh, D.-B. Park, S.-M. Hong, J.-H. Shim, et al., Effect of Nb and Cu on the high temperature creep properties of a high Mn–N austenitic stainless steel, Mater. Charact. 83 (2013) 49–57. doi:10.1016/j.matchar.2013.05.015.

[13] H.K. Danielsen, J. Hald, On the nucleation and dissolution process of Z-phase Cr(V,Nb)N in martensitic 12%Cr steels, Mater. Sci. Eng. A. 505 (2009) 169–177. doi:10.1016/j.msea.2008.11.019.

[14] L. Cipolla, H.K. Danielsen, D. Venditti, P.E. Di Nunzio, J. Hald, M.A.J. Somers, Conversion of MX nitrides to Z-phase in a martensitic 12% Cr steel, Acta Mater. 58 (2010) 669–679. doi:10.1016/j.actamat.2009.09.045.

[15] F. Masuyama and P.R. Boyles, Effect of Service Exposure on Material Properties of Austenitic Boiler Steels, in: ASME 2007 Press. Vessel. Pip. Conf., San Antonio, Texas, 2007: pp. 617–622.

[16] S. Latha, M.D. Mathew, P. Parameswaran, K. Bhanu Sankara Rao, S.L. Mannan, Thermal creep properties of alloy D9 stainless steel and 316 stainless steel fuel clad tubes, Int. J. Press. Vessel. Pip. 85 (2008) 866–870. doi:10.1016/j.ijpvp.2008.07.002.

[17] T.G. Langdon, Grain boundary sliding as a deformation mechanism during creep, Philos. Mag. 22 (1970) 689–700. doi:10.1080/14786437008220939.

[18] S. Xu, A.K. Koul, J.I. Dickson, Creep crack growth in the absence of grain boundary precipitates in UDIMET 520, Metall. Mater. Trans. A. 32 (2001) 795–804. doi:10.1007/s11661-001-0095-9.

[19] S. Xu, X.-J. Wu, A.K. Koul, J.I. Dickson, An intergranular creep crack growth model based on grain boundary sliding, Metall. Mater. Trans. A. 30 (1999) 1039–1045. doi:10.1007/s11661-999-0156-z.

[20] X.J. Wu, A.K. Koul, Grain boundary sliding in the presence of grain boundary precipitates during transient creep, Metall. Mater. Trans. A. 26 (1995) 905–914. doi:10.1007/BF02649087.

[21] K. Laha, J. Kyono, T. Sasaki, S. Kishimoto, N. Shinya, Improved creep strength and creep ductility of type 347 austenitic stainless steel through the self-healing effect of boron for creep cavitation, Metall. Mater. Trans. A. 36 (2005) 399–409. doi:10.1007/s11661-005-0311-0.

[22] M.E. Kassner, Creep Behavior of Particle-Strengthened Alloys, 2nd ed., Elsevier, 2009. doi:10.1016/B978-0-08-047561-5.00010-5.

[23] S. Kim, S. Lee, Y. Oshima, Y. Kondo, E. Okunishi, N. Endo, et al., Scanning moiré fringe imaging for quantitative strain mapping in semiconductor devices, Appl. Phys. Lett. 102 (2013). doi:10.1063/1.4803087.

[24] L.K. Singhal, J.W. Martin, The formation of ferrite and sigma-phase in some austenitic stainless steels, Acta Metall. 16 (1968) 1441–1451. doi:10.1016/0001-6160(68)90039-4.

[25] H.E. Evans, The mechanism of void growth and factors affecting the onset of intergranular failure during creep of a Mg–0·8% Al alloy, Met. Sci. J. 3 (1969) 33–38. doi:10.1179/msc.1969.3.1.33.

[26] W. Beere, Models of creep cavitation and their interrelationships, Scr. Metall. 17 (1983) 13–16. doi:10.1016/0036-9748(83)90062-5.

[27] S. Mahesh, K.C. Alur, M.D. Mathew, A creep model for austenitic stainless steels incorporating cavitation and wedge cracking, Model. Simul. Mater. Sci. Eng. 19 (2011). doi:10.1088/0965-0393/19/1/015005.

[28] W.D. Nix, Mechanisms and controlling factors in creep fracture, Mater. Sci. Eng. A. 103 (1988) 103–110. doi:10.1016/0025-5416(88)90556-3.

[29] W.D. Nix, K.S. Yu, J.S. Wang, The effects of segregation on the kinetics of irrtergranular cavity growth under creep conditions, Metall. Trans. A. 14 (1983) 563–570. doi:10.1007/BF02643773.

[30] D. Young, Internal oxidation processes under non-ideal conditions, Mater. High Temp. 17 (2000) 465 – 470.

[31] J. Erneman, M. Schwind, P. Liu, J.O. Nilsson, H.-O. Andrén, J. Ågren, Precipitation reactions caused by nitrogen uptake during service at high temperatures of a niobium stabilised austenitic stainless steel, Acta Mater. 52 (2004) 4337–4350. doi:10.1016/j.actamat.2004.06.001.